Detection of aldehydes from degradation of lipid nanoparticle formulations using a hierarchically-organized nanopore electrochemical biosensor

Julius Reitemeier,[a] Jarek Metro,[a] and Paul W. Bohn[*a, b]

a Department of Chemistry and Biochemistry, University of Notre Dame, Notre Dame, Indiana 46556, United States

b Department of Chemical and Biomolecular Engineering, University of Notre Dame, Notre Dame, Indiana 46556, United States

[*]Author to whom correspondence should be addressed: *pbohn@nd.edu*

Abstract

Degradation of ionizable lipids in mRNA-based vaccines was recently found to deactivate the payload, demanding rigorous monitoring of impurities in lipid nanoparticle (LNP) formulations. However, parallel screening for lipid degradation in customized delivery systems for next-generation therapeutics maintains a challenging and unsolved problem. Here, we describe a nanopore electrochemical sensor to detect ppb-levels of aldehydes arising from lipid degradation in LNP formulations that can be deployed in massively parallel fashion. Specifically, we combine nanopore electrodes with a block copolymer (BCP) membrane capable of hydrophobic gating of analyte transport between the bulk solution and the nanopore volume. By incorporating aldehyde dehydrogenase (ALDH), enzymatic oxidation of aldehydes generates NADH to enable ultrasensitive voltammetric detection with limits-of-detection (LOD) down to 1.2 ppb. Sensor utility was demonstrated by detecting degradation of N-oxidized SM-102, the ionizable lipid in Moderna's SpikeVax^{TM} vaccine, in mRNA-1273 LNP formulation. This work should be of significant use in the pharmaceutical industry, paving the way for automated on-line quality assessments of next-generation therapeutics.

1. Introduction

Messenger ribonucleic acid (mRNA)-vaccines from Pfizer/BioNTech and Moderna played a pivotal role in fighting the SARS-CoV-2 virus, as they demonstrated sufficient efficacy and safety for emergency use authorization by the FDA (Baden et al., 2020; Polack et al., 2020). By encapsulating mRNA inside lipid nanoparticle (LNP) delivery systems, the stability of mRNA cargo improves significantly, preventing degradation of the nucleic acids (Pardi et al., 2015; Reichmuth et al., 2016) and promoting cellular uptake (Cullis and Hope, 2017). However, mRNA

is prone to oxidation, hydrolysis, or transesterification (Houseley and Tollervey, 2009; Pogocki and Schöneich, 2000), requiring well-controlled chemical environments, *i.e.*, lipid composition, storage temperature, buffers, and pH (Oude Blenke et al., 2023; Schoenmaker et al., 2021), during storage. To avoid the build-up of degradation products in therapeutics, the chemical stability of LNP formulations has been identified as a critical quality attribute (CQA) by the FDA (U.S. Food & Drug Administration, 2018), demanding rigorous monitoring of oxidative impurities in lipid delivery systems under various storage conditions.

Generally, LNP formulations are composed of lipids from four classes: phospholipids, structural helper lipids, *e.g.*, cholesterol, PEGylated-lipids, and ionizable lipids (Hald Albertsen et al., 2022), with the latter class representing the most crucial component, because it encapsulates mRNA inside the lipid shell and facilitates discharge of the payload during the endosomal escape pathway (Eygeris et al., 2022; Hou et al., 2021). The emergence of LNP-based mRNA formulations as next-generation therapeutics for cancer immunotherapy (Estapé Senti et al., 2024; Guevara et al., 2020) has resulted in increasingly complex lipid delivery systems, fueling the need for sensitive, rapid, and high-throughput point-of-use sensors for the detection of lipid degradation products in customized formulations. For example, a novel mechanism of mRNA deactivation, caused by the degradation of ionizable lipids, was recently discovered by Packer, *et al*. who observed degradation initiated by N-oxidation at the tertiary amine and subsequent hydrolysis to the aldehyde (Packer et al., 2021). The current analytical gold standard for detecting lipid degradation involves liquid chromatography coupled with mass spectrometry (LC-MS) (Birdsall et al., 2024; Fan et al., 2021; Reinhart et al., 2023; Siriwardane et al., 2020), however, these methods involve time-intensive sample preparation, chemical modification of the target, off-line usage, and high costs. Therefore, easy-to-use spectroscopic methods such as corona charged

aerosol detection (CAD) and evaporative light scattering detection (ELSD) (Jeschek et al., 2016; Kinsey et al., 2022; Zhong et al., 2010) have been developed as alternatives to mass spectrometry, but these techniques do not meet the required sensitivity standards for all cases (Birdsall et al., 2024; Vervoort et al., 2008).

In this work, we demonstrate a novel hydrophobically-gated, hierarchically-organized nanopore electrochemical sensor that is capable of sensitive, label-free, and *in situ* detection of aldehyde degradation products in LNP formulations in multiplex fashion. This sensor addresses a number of technical challenges, specifically: (*a*) capturing and trapping small molecule analytes from bulk solution, (*b*) enhancing the sensitivity of voltammetric measurements, (*c*) improving the selectivity of inherently non-selective electrochemical measurements, (*d*) eliminating the large overpotential for NADH oxidation, and (*e*) extending the range of aldehydes that could be measured. These objectives were accomplished using nanopore electrode arrays (NEAs), which are massively parallel arrays of nanopores with one or multiple recessed electrodes, to take advantage of volume confinement enhancements to electrochemical detection (Baek et al., 2022). Here, we utilize NEAs hosting two recessed electrodes, **Fig. 1a**, which exploit the electroanalytical advantages arising from ultrasmall volumes and enable sensitive voltammetric readouts (Arrigan, 2004; Fu et al., 2020). A block copolymer (BCP) membrane, consisting of two or more homopolymers arranged in linear blocks, is placed on top of the NEAs, yielding hierarchically-organized BCP@NEA structures. The self-assembly of BCP membranes into well-defined geometries is exploited by utilizing poly(styrene)-*block*-poly(4-vinyl)pyridine (PS-*b*-P4VP), which undergoes phase segregation into vertically-aligned hydrophobic nanochannels and enables stimulus-responsive gating to control transmembrane transport (Liu et al., 2016; Reitemeier et al., 2023). Initially, the nanochannels are dewetted, thus blocking transport of

aqueous solution components. Upon application of an external bias, the nanochannels undergo a transition to a wetted state, which then allows the solution to pass through the cylindrical BCP nanopores (Powell et al., 2011; Smirnov et al., 2011). The small size of the asymmetric BCP nanochannels (~10 nm) (Yu et al., 2015) prevents larger entities from reaching the nanopore electrodes while allowing passage of smaller solutes across the BCP membrane. In addition, the reversible electrowetting/dewetting transition makes it possible to turn off transport and confine the captured species in the attoliter (10^{-18} L) pore volume of the NEA vestibule (Reitemeier et al., 2023). The latter effect is known to influence enzyme efficacy as a result of crowding and has been shown to increase enzyme activity in electrochemical sensors (Küchler et al., 2016; Wang et al., 2012).

To enable the electrochemical detection of aldehydes, the NAD-dependent enzyme aldehyde dehydrogenase (ALDH) is immobilized inside the nanopores, and freely-diffusing NAD^+ is added. Electroactive NADH is produced during the conversion of aldehyde substrates to the corresponding carboxylic acid, the NADH then being detected using square wave voltammetry (SWV). The capabilities of the aldehyde sensor are demonstrated by detecting small aliphatic and aromatic aldehydes with limits-of-detection (LODs) down to 1.2 ppb, outperforming conventional 2,4-dinitrophenylhydrazine (DNPH)-tagged LC-MS assays for the detection of aldehydes by several orders of magnitude (Chi et al., 2007; Douny et al., 2016; Douny et al., 2015; Melo Cardozo et al., 2020; Wang et al., 2022). Finally, the real-world applicability of the sensor was tested by detecting the degradation products of SM-102 N-oxide in the FDA-approved mRNA-1273 LNP formulation, achieving a 650 ppb LOD. This work represents a breakthrough in therapeutic drug screening, enabling the rapid (~5 min), sensitive, and high-throughput detection of lipid

degradation to overcome the challenges of parallel LNP quality assessments for next-generation lipid-based therapeutics.

2. Results and Discussion

2.1 Design and characterization of hierarchically-organized BCP@NEA sensors

Electrochemical chips hosting eight individually addressable hierarchically-organized BCP@NEA elements were designed, **Fig. 1b**, with NEAs containing up to 55,000 nanopores/array (**Fig. S1**) serving as the electroanalytical platform. Each nanopore houses two recessed Au electrodes separated by an electrically insulating SiN_X dielectric layer. This design allows for independent electrode operation, with the bottom electrode serving as a sensing electrode (S) and the top electrode serving both as a gating electrode (G) to control hydrophobic gating and as a platform for immobilization of the ALDH enzyme, *viz.* **Fig. 1a**. A polystyrene-*b*-poly(4-vinyl)pyridine (PS-*b*-P4VP) BCP membrane was placed onto the NEAs using a biocompatible sacrificial layer transfer strategy to encapsulate a ~50 aL individual pores in the NEA. The structural integrity of the architecture was validated using cross-sectional scanning electron microscopy (SEM), **Fig. 1c**, showing that the PS-*b*-P4VP membrane adheres to the NEA layer without intrusion into the underlying nanopores. A top-view SEM image of the structure reveals the self-assembly of vertically-aligned P4VP nanochannels, **Fig. 1d**, showing a dense packed array of transmembrane channels with average diameter 14 nm and average pitch 41 nm. Given the nanopore electrode density of 5.5 pores/μm^2, each NEA nanopore is in fluidic communication with ~83 BCP nanochannels.

To test that mass transport across the polymeric feature is blocked in its resting, dewetted state, cyclic voltammetry (CV) of a redox probe, $Fe(CN)_6^{3/4-}$, was obtained at the underlying NEA before and after application of a PS-*b*-P4VP membrane, **Fig. 1e**. Open, uncovered NEAs exhibit i-V responses characteristic of diffusion-limited transport, demonstrating unhindered diffusion of redox molecules from the bulk solution into the nanopores containing the NEA electrodes. In contrast, in the presence of the BCP membrane, the overall current decreases dramatically, yielding only non-faradaic charging current. The change in CV behavior is consistent with the efficient blockage of transmembrane transport when the PS-*b*-P4VP membrane is in its dewetted state, leading to the effective isolation of the nanopore volume from the bulk solution.

2.2 Potential-induced hydrophobic gating of BCP@NEA devices

External control of the hydrophobic gating characteristics of the BCP membrane was characterized as a function of potential bias and solvent composition, since LNPs are typically formulated in an organic/aqueous solvent mixture (Musielak et al., 2022). First, the transition from dewetted-to-wetted state of a PS-*b*-P4VP membrane covering a planar Au electrode was characterized by cycling the electrode potential in solutions containing varying volumetric ratios of acetonitrile:PBS, **Fig. 2a**. When cycling the potential of the electrode from 0.0 V to strongly negative potentials *vs*. Ag/AgCl, a current threshold is observed, indicating the gating of flux across the membrane to the electrode, consistent with the transition of the BCP channels from a dewetted to a wetted state. The current hysteresis observed on the backward scan indicates a voltage offset between the potential at which the nanochannels are wetted and the subsequent potential-dependent restoration of their dewetted state. Similarly, when using ethanol:PBS solvent

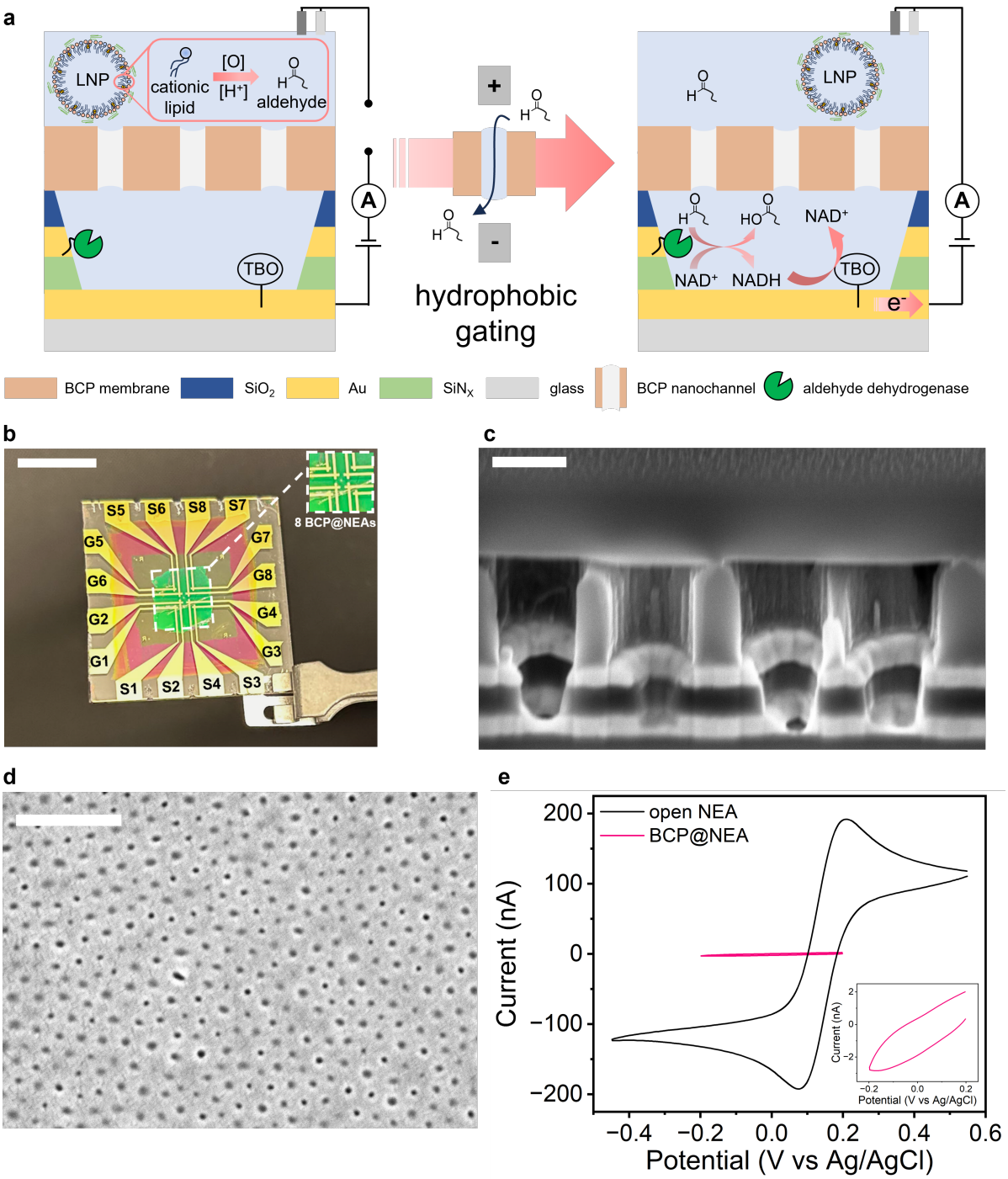

Fig. 1. Hierarchically-organized BCP@NEA sensors. **a.** Schematic representation of the enzyme-coupled detection of aldehyde degradation products. **b.** Optical image of a device hosting eight individual BCP@NEA sensing elements. Electrode connector pads for gating (G) and sensing (S) electrodes for each BCP@NEA are marked. Scale bar indicates 10 mm. **c.** Cross-sectional SEM image of four parallel electrochemically active PS-*b*-P4VP covered nanopores. Light areas are Au, and featureless area at top is the BCP membrane. Scale bar indicates 250 nm. **d.** Plan-view SEM image of the vertically-aligned nanochannels of a PS-*b*-P4VP membrane after transfer onto an NEA device. Scale bar indicates 200 nm. **e.** CVs of 5 mM $Fe(CN)_6^{3-}$ in PBS in an NEA device before and after application of PS-*b*-P4VP membrane. Inset: Magnified (100×) BCP@NEA current trace.

mixtures, larger potential biases are required to initiate wetting (**Fig. S2**), consistent with the higher energy barrier for electrowetting of the hydrophobic wall by ethanol:PBS compared to pure PBS or acetonitrile:PBS mixtures, as the surface tension increases with solvent polarity (Smirnov et al., 2011).

To investigate the potential-dependent gating behavior for BCP@NEA architectures, discrete potential pulses were applied on the gating electrode and the current transients were observed, **Fig. 2b**. Plateau currents are steady at applied potentials, $E_{appl} > -0.6$ V *vs*. Ag/AgCl, but at $E_{appl} \leq -0.6$ V, the current exhibits a strong increase, that is attributed to dynamic wetting of the BCP nanochannels enhancing the flux of $Fe(CN)_6^{3/4-}$ redox probe to the NEA electrodes, thus establishing potential-induced gating of the BCP membrane. Three distinct phases are observed: (1) a dewetted state exhibiting minimal mass transport at $-0.1 \text{ V} \geq E_{appl} \geq -0.6$ V; (2) a dynamically wetted pore ensemble at $-0.6 \text{ V} \geq E_{appl} \geq -0.9$ V with onset of significant transport across the BCP nanochannels; and (3) fully wetted nanochannels at $E_{appl} \leq -0.9$ V supporting strong fluidic coupling between bulk solution and the vestibules of the NEA nanopores.

In order to compare potential-induced wetting behavior for solutions of varying polarity, a characteristic switching potential E_S is defined as the point at which 50% of the steady-state current is reached. To extract the switching potential, the faradaic currents obtained in acetontirile:PBS solvent mixtures are plotted against potential, **Fig. 2c**, and the switching potential, obtained as the inflection point of a fit of the i-V curves, is plotted against the organic solvent content for both ethanol and acetonitrile mixtures, **Fig. 2d**. Comparing the behavior of acetontrile:PBS to ethanol:PBS, the switching occurs at more positive E_S values for acetontrile:PBS mixtures of the same organic content, since solvent mixtures of lower polarity exhibit a lower potential barrier to hydrophobic-gating.

Finally, the ability to exploit electrowetting transitions to capture redox probe species from the bulk solution and confine them inside the NEA nanopores was tested. The potential of the gating electrode was poised to the E_S value appropriate for the solvent composition for 30 s to allow sufficient time for transmembrane transport, after which the potential was switched back to a sufficiently positive value to dewet the BCP nanopores. Afterward, the confinement of redox probes was tested by acquiring CVs. The CVs exhibit typical thin-layer cell (TLC) behavior as evidenced by two observations: (1) as shown in **Fig. 2e**, the anodic and cathodic peaks occur at nearly the same value, *i.e.*, ~ 5 mV peak separation, well below the expected ~59 mV for Nernstian freely-diffusing conditions (Bard et al., 2022), and (2) the anodic and cathodic peak currents vary linearly with scan rate, **Fig. 2f**. The observation of TLC behavior in the NEA nanopores supports the interpretation of reversible wetting/dewetting behavior of BCP nanochannels in solvents with up to 20% acetonitrile. Similar behavior is observed in ethanol:PBS mixtures with up to 20% ethanol (**Fig. S3**). Intriguingly, when using 50% acetonitrile, the voltammograms display diffusion-limited transport characteristics (**Fig. S4**). This behavior is consistent with facile fluidic communication with the bulk of solutions, such as would be observed upon loss of confinement.

2.3 Electrochemical NADH mediation and aldehyde sensing on BCP@NEAs

After characterizing the hydrophobic gating properties of the BCP@NEA structures, the ALDH-coupled detection of aldehydes was investigated. To avoid large overpotentials for the oxidation of NADH on Au electrodes (Moiroux and Elving, 1980), *p*-toluidine blue (TBO) was chosen as a redox mediator based on the facile two-electron transfer kinetics of phenothiazines with NADH (Gligor et al., 2009; Ohtani et al., 1997). In order to selectively immobilize the mediator on the sensing electrode, the diazo-TBO compound was generated in a one-step nitrosylation reaction, then electrochemically grafted onto the sensing electrode by applying a

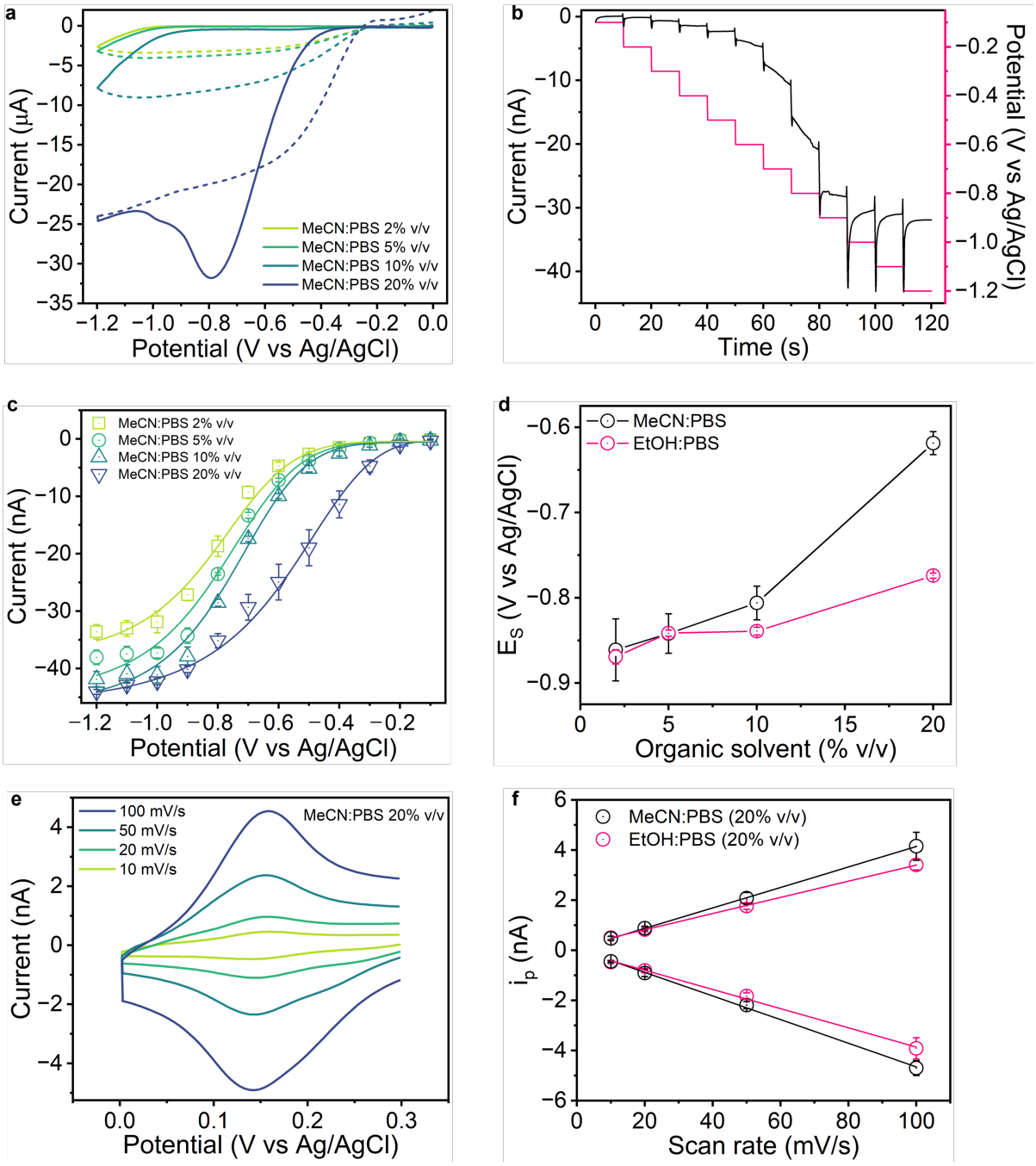

Fig. 2. Potential-induced hydrophobic gating of PS-*b*-P4VP membranes. **a.** CVs of 5 mM $Fe(CN)_6^{3-/4-}$ in varying volumetric ratios of acetonitrile:PBS on a BCP-covered planar Au electrode. **b.** Chronoamperometry (black, left axis) in response to a staircase potential (magenta, right axis) on the gating electrode of a BCP@NEA device. **c.** Current-potential relations from a BCP@NEA device as a function of the volumetric ratio of acetonitrile. **d.** Change in switching potential, E_S, as a function of acetonitrile and ethanol content using BCP@NEA devices. **e.** CVs collected after hydrophobic gating on a BCP@NEA device in 20% v/v acetonitrile with varying scan rates. **f.** Peak current, i_p, as a function of scan rate obtained after hydrophobic gating in 20% v/v acetonitrile and ethanol, respectively. Error bars indicate standard deviations across n = 3 replicates.

constant reducing potential of -0.6 V *vs*. Ag/AgCl (**Fig. S5**). The electrode modification was characterized using infrared spectroscopy (**Fig. S6**) and the adsorbate coverage was determined using CV at varying scan rates (**Fig. S7**), yielding a TBO coverage of ~ (5.67 ± 0.04) × 10^{-11} mol/cm^2. The electrocatalytic activity for the oxidation of NADH was demonstrated on a TBO-modified planar Au (pAu) electrode, **Fig. 3a**, showing efficient oxidation of NADH as an irreversible anodic wave.

Square wave voltammetry, a differential AC pulse voltammetric measurement method that yields superior signal-to-noise ratios in short assay times (Bard et al., 2022), was utilized to optimize anodic detection of NADH. The efficient redox mediation of NADH on a TBO-modified gold electrode was investigated empirically as a function of frequency and amplitude of the applied square wave. Square wave voltammograms of solutions containing varying concentrations of NADH were recorded, showing a peak at ~ 0.15 V that correlates with the analyte concentration (**Fig. S8**). Notably, a second peak at ~ -0.20 V can be attributed to the reduction of dissolved oxygen in solution, which shows up as an anodic peak due to the differential nature of SWV and can be observed throughout subsequent measurements. The LODs obtained from these measurements for the detection of NADH using 12 permutations of frequency and amplitude are shown in **Fig. 3b**, demonstrating that a combination of 100 mV and 50 Hz results in the lowest LOD.

Next, the BCP@NEA aldehyde sensor was assembled. Redox mediator TBO was selectively grafted onto the sensing electrode, while ALDH was covalently immobilized onto both electrodes, and a PS-*b*-P4VP membrane was mounted to the NEA structure to yield the fully functional BCP@NEA sensor architecture. The sensing capabilities were initially tested

using benzaldehyde, a known substrate for the yeast ALDH enzyme used in these studies (Wang et al., 2009). Sensing reactions were initiated using hydrophobic gating to introduce and capture the target aldehyde. Subsequent enzymatic reaction with the analyte resulted in accumulation of NADH inside the NEA vestibule, which was detected via SWV, **Fig. 3c**, revealing strong correlation between the anodic NADH peak current at 0.15 V vs Ag/AgCl and the benzaldehyde concentration. The corresponding working curve, **Fig. 3d**, exhibits a dynamic response from 100 nM to 10 mM, with an LOD of 11 nM, *i.e.*, 1.2 ppb for benzaldehyde. The log-linear response curve is characteristic for an electrocatalytic sensing scheme and ultimately reflects the underlying ALDH kinetics. Sensing experiments conducted with acetaldehyde (**Fig. S9**) yielded a similar response with an LOD of 89 nM, *i.e.*, 3.9 ppb. To further investigate the sensing performance, we conducted sensing experiments for acetaldehyde without a BCP membrane, **Fig. S10**. Voltammograms obtained without the BCP membrane exhibit significantly lower sensitivity, *e.g.*, an LOD of ~1.3 μM compared to BCP@NEA sensors. We attribute the enhanced sensing performances in BCP@NEA geometries to a combination of two effects: (1) A concentration enrichment based on the entrapment of NADH, and (2) an increase in enzyme activity resulting from the strong attoliter-volume confinement.

To investigate the selectivity of the sensor toward aldehydes of various structures, the sensor response was characterized with aromatic, aliphatic, and unsaturated substrates, **Fig. 3e**. Smaller aromatic aldehydes, benzaldehyde and 5-hydroxymethylfurfural (5-HMF), yield similar peak currents, indicating high enzymatic turnover. Aliphatic aldehydes exhibit decreasing signals with increasing chain length, with acetaldehyde (C2) peak currents being comparable to those of

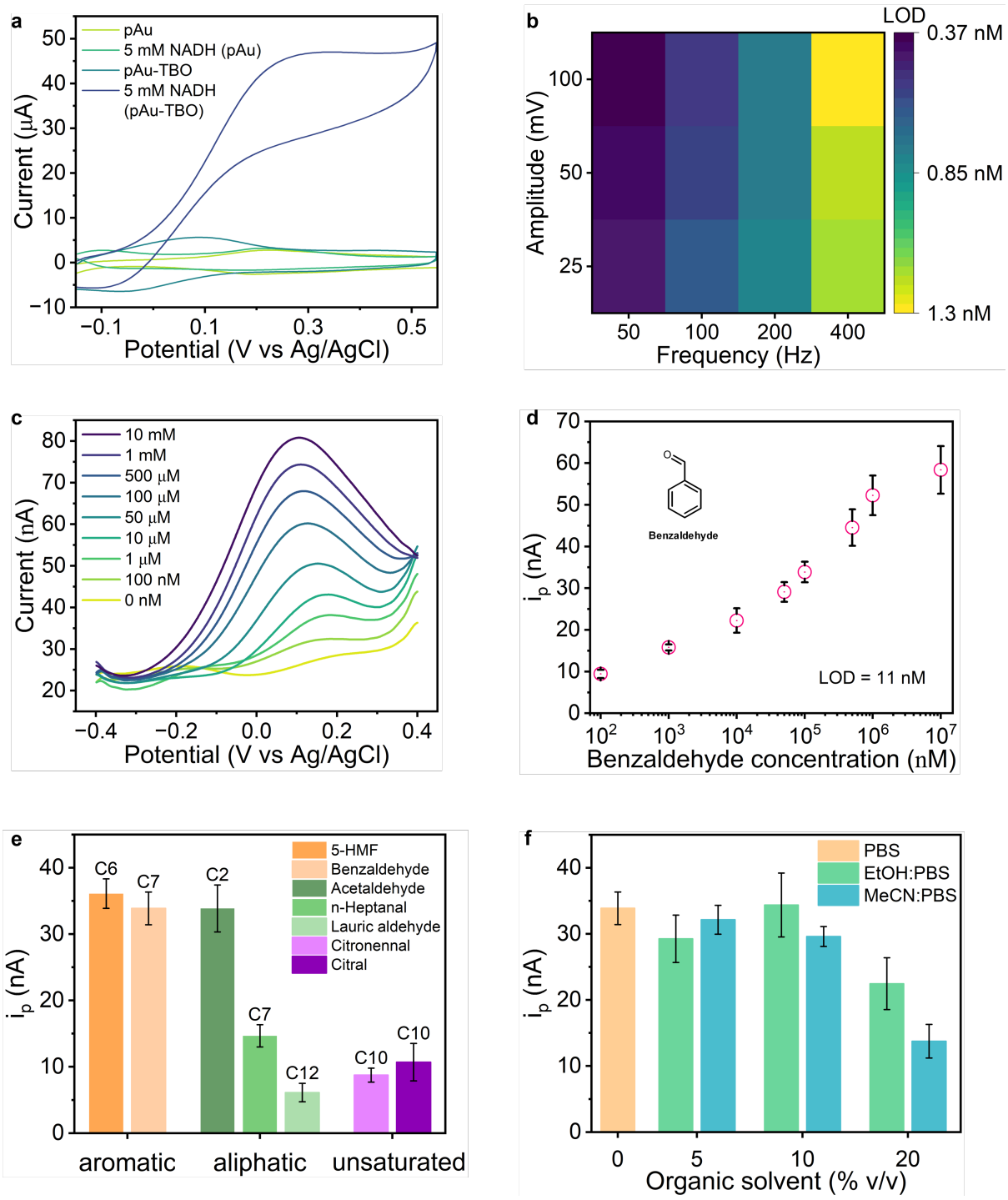

Fig. 3. Aldehyde detection in ALDH-functionalized BCP@NEA devices. **a.** CVs before and after electrografting of TBO on a pAu electrode in the presence and absence of 5 mM NADH. **b.** Limit-of-detection heatmap for the detection of NADH using SWV for 12 different amplitude/frequency pairs. **c.** SWVs collected after hydrophobic gating of varying benzaldehyde solutions on ALDH-functionalized BCP@NEAs. **d.** Working curve obtained for the detection of benzaldehyde on BCP@NEA devices across five orders of magnitude in aldehyde concentration. **e.** Current responses obtained upon incubation of 100 μM solution of various aldehydes. **f.** Sensor performance in various non-aqueous solvent mixtures of ethanol and acetonitrile in PBS containing 100 μM benzaldehyde. Error bars indicate the standard deviation across n = 3 replicates.

smaller aromatic aldehydes, while the responses from n-heptanal (C7) and lauric aldehyde (C12) show that signal decreases strongly with aliphatic chain length. Similarly, the sensor yields diminished currents for citronennal and citral, which are of equal chain length, but differ in the degree of unsaturation. Sensing performance was also tested using benzaldehyde in varying volumetric ratios of the organic co-solvents ethanol and acetonitrile, **Fig. 3f**. The sensor shows approximately constant performance in up to 10% volumetric ratios of both ethanol and acetonitrile in PBS. However, the current drops *ca.* 2-fold going from 10% to 20% organic content.

2.4 SM-102 N-oxide degradation in mRNA-1273 LNP formulations

As recently discovered by Packer *et al*. (Packer et al., 2021), N-oxidized ionizable lipids undergo hydrolysis in slightly acidic media, producing secondary amine and aldehyde decomposition products, **Fig. 4a**. To test the capability of BCP@NEA sensors to detect aldehyde decomposition products in realistic conditions, the degradation of N-oxidized SM-102, an ionizable lipid used in the mRNA-1273 (SpikeVax^{TM}) LNP vaccine from Moderna (Hassett et al., 2019; Schoenmaker et al., 2021), was investigated in acetate buffer at pH = 5.3, *i.e.*, under raw LNP synthesis conditions. The structure of SM-102, **Fig. 4b**, consists of two long- and one short-chain alkyl substituents attached to the tertiary amine. Based on the acidic hydrolysis pathway, the degradation of SM-102 N-oxide results in all three corresponding aldehydes (Packer et al., 2021), however, because of the sensor's selectivity toward short-chained aliphatic aldehydes, the short-chain product, hydroxyacetaldehyde, **Fig. 4c**, is expected to dominate the response.

LNPs were synthesized following the FDA approved mRNA-1273 lipid formulation, and characterized using dynamic light scattering, **Fig. 4d**, which yielded an average diameter of ~219 nm with a polydispersity index PDI = 0.1 and a zeta-potential ζ = -15.5 mV. The LNP solutions

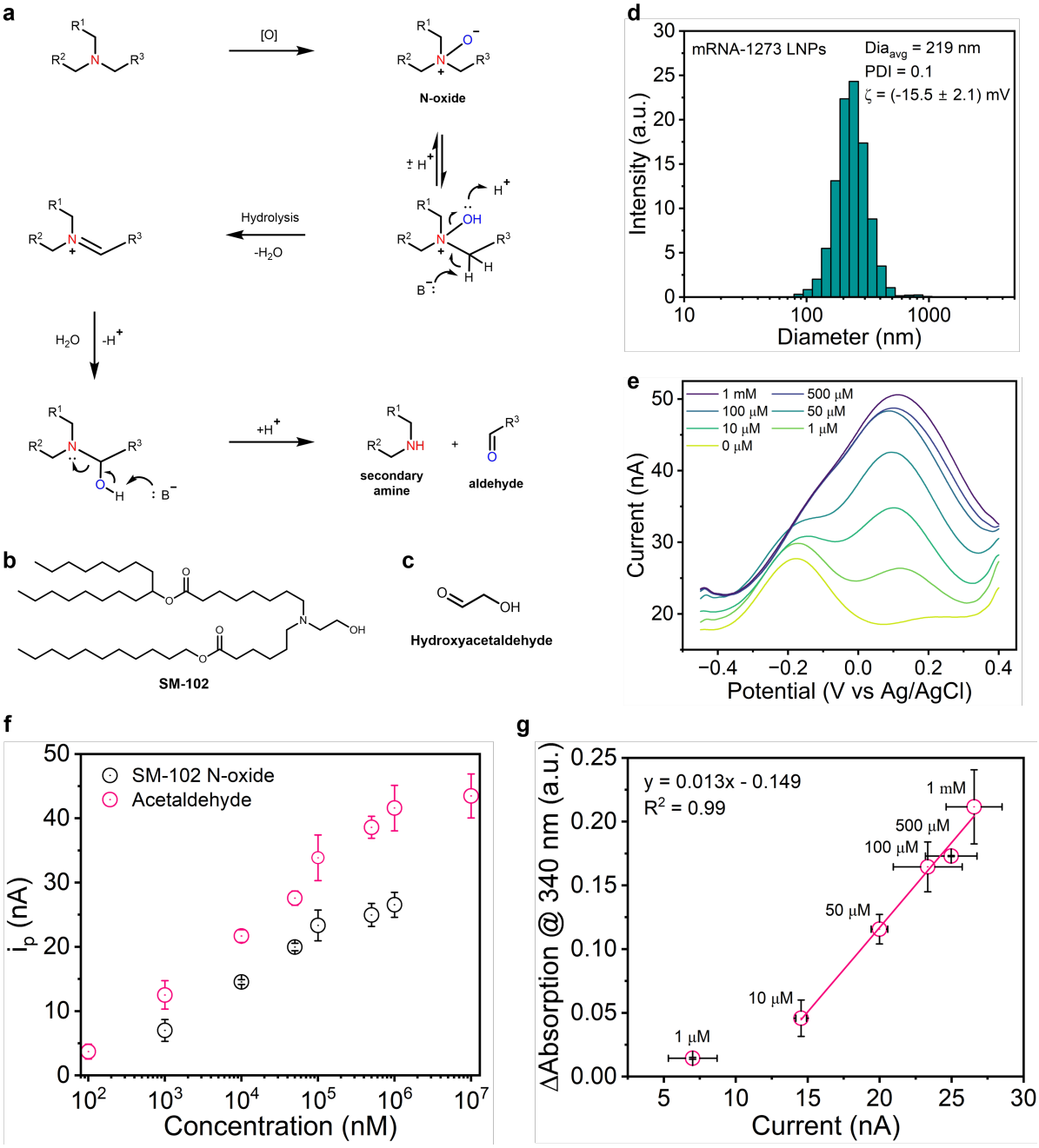

Fig. 4. Electrochemical detection of degradation products in LNP formulations using BCP@NEA sensors. **a.** Degradation pathway for ionizable lipids after N-oxidation and hydrolysis. **b.** The ionizable lipid SM-102 used in the mRNA-1273 LNP formulation. **c.** Hydroxyacetaldehyde, a short-chained aliphatic degradation product. **d.** Dynamic light scattering (DLS) results for synthesized LNPs following the mRNA-1273 lipid formulation. **e.** SWVs on a BCP@NEA device obtained from spiked LNP solutions containing varying concentrations of degraded SM-102 N-oxide. **f.** Working curves obtained for SM-102 N-oxide degradation and acetaldehyde using BCP@NEA devices. **g.** Cross-validation curve for the detection of SM-102 N-oxide degradation products using the BCP@NEA sensor and ALDH-coupled UV-vis absorption assay. Error bars indicate the standard deviation across n = 3 replicates.

were spiked with SM-102 N-oxide solution that had been degraded for 7 d at 300 K. To detect aldehyde degradation products, spiked LNP solutions were measured on BCP@NEA sensors, and the aldehydes were detected using SWV, **Fig. 4e**. The voltammograms show the typical peak current at ~ 0.15 V vs Ag/AgCl for the enzymatic product NADH which correlates in magnitude with the concentration of degraded SM-102 N-oxide. A working curve was generated and compared to that of acetaldehyde, an aliphatic aldehyde with similar chain length, **Fig. 4f**. The SM-102 N-oxide working curve is linear from 1 μM – 100 μM and saturates at higher concentrations, which can be attributed, in part, to the dimerization of the hydroxyacetaldehyde to non-carbonyl structures at higher concentrations (Collins and George, 1971). Furthermore, the working curve exhibits an LOD ~ 900 nM for the degradation of SM-102 N-oxide, a ~10-fold decrease in sensitivity compared to acetaldehyde (~ 89 nM), an observation that can be ascribed to a combination of (1) the statistical mixture containing hydroxyacetaldehyde at a ratio of 1/3 relative to the parent N-oxide, and (2) chemical cross-reactivity and partitioning between the lipid shell and the bulk solution further decreasing the effective concentration.

Finally, to validate the sensing performance of the BCP@NEA sensor toward aldehyde degradation products in SM-102 N-oxide solution, ALDH-coupled UV-vis spectrophotometry assays were utilized. Monitoring generation of NADH by two independent assays cross-validates the detection of short-chained aldehydes from SM-102 N-oxide degradation. Typical UV-vis spectra obtained upon incubation of degraded SM-102 N-oxide over time are shown in **Fig. S11**. The resulting change in absorbance at 340 nm, the absorbance maximum for enzymatically generated NADH, after 30 min was used to cross-validate the current response obtained using the BCP@NEA sensor, **Fig. 4g**, demonstrating a high degree of correlation between the independent

analytical methods in the concentration range 10 μM - 1 mM, limited at the low concentration end by the sensitivity of UV-vis assay for NADH.

3. Conclusions

The hierarchically-organized BCP@NEA sensors developed here provide a framework for the sensitive and *in situ* quality assessment throughout long-term storage and use of LNP formulations for the delivery of therapeutics and vaccines - a key technological hurdle for the development of personalized dosing strategies. The approach developed here is based on a hydrophobically-gated electrochemical biosensor that is capable of capturing, then trapping, analytes of interest, *i.e.*, oxidized (aldehyde) impurities produced as degradation products from oxidation, then hydrolysis, of ionizable lipids in the test case studied here. The resulting sensor, based on rugged, inexpensive enzyme-linked voltammetric measurements, is ideally suited to the characterization of large numbers of small batch therapeutics and has the potential for automated operation in parallel fashion. It is robust, sensitive, selective, and capable of operation in organic:PBS mixed solvent systems. In addition, its target range may readily be extended by incorporating alternative ALDHs, *e.g.*, those obtained from organisms other than yeast, such as human dehydrogenases. Key technological advances include optimized sensitivity and selectivity in voltammetric measurements of aldehydes, achieving LODs as low as 1.2 ppb. The innovations introduced here enhance the sensor's practical utility for detecting a broad range of aldehyde impurities, including those from degraded ionizable lipids, *e.g.,* SM-102, as demonstrated in this work.

The proof-of-principle prototypes developed here can be readily extended to multiplex determinations and point-of-use measurements. For example, incorporating eight individual sensing elements on a single lab-on-a-chip device takes advantage of the small spatial footprint of the sensor and enables high throughput, on-line integration into parallel product streams for multiplex point-of-use testing and quality assessments under different storage conditions. Other ionizable lipids, *e.g.*, ALC-0315, which bears a hydroxybutanyl substituent at the tertiary amine, are expected to generate sensitive responses based on the selectivity of the sensor for smaller aldehydes. For larger aliphatic substituents, the incorporation of other dehydrogenases, such as the human enzyme families ALDHA1 or ALDHA3, that can convert large, long-chained aldehydes, may improve the sensitivity toward larger substrates. Furthermore, the simplicity of the electrochemical measurements minimizes the need for expensive and highly specialized equipment meaning that the sensor holds great potential for automated operation. These findings have significant potential for the pharmaceutical industry, because they address a strategy for massively parallel sensing of chemical impurities in next-generation LNP-based therapeutics, and, as such, they should play a substantial role in advancing technologies for manufacture of personalized therapeutics.

4. Materials and methods

4.1 Reagents

1,4-Dioxane, 1-ethyl-3-(3-dimethylaminopropyl)carbodiimide (EDC), 3-mercaptopropionic acid (3-MPA), 5-hydroxymethylfurfural (5-HMF), acetaldehyde, acetic acid, acetone, acetonitrile, aldehyde dehydrogenase (ALDH) potassium-activated from yeast (>10

units/mg protein, EC number: 1.2.1.5) , benzaldehyde, cholesterol, citral, citronennal, dialysis tubing (MWCO = 12.400 Da), ethyl alcohol, hydrochloric acid, lauric aldehyde, n-heptanal, N-hydroxy succinimide, phosphate buffered saline (PBS) pH = 7.4, poly(acrylic acid) solution (MW ~ 100,000, 35 wt.% in H2O), polystyrene latex beads (0.46 μm mean particle size), potassium acetate, potassium ferricyanide(III) ($K_3Fe(CN)_6$), potassium ferrocyanide(IV) ($K_4Fe(CN)_6$), *p*-toluidine blue (TBO), sodium nitrite, sulfuric acid (conc.), β-nicotinamide adenine dinucleotide hydrate (NAD+), and β-nicotinamide adenine dinucleotide, reduced disodium salt hydrate (NADH) were purchased from Sigma-Aldrich, USA. 1,2-Dimeryristoyl-rac-glycero-3-methoxypolyethylene glycol-2000 (DMG-PEG(2000)), 1,2-distearoyl-sn-glcero-3-PC (1,2-DSPC), 8-[(2-hydroxyethyl)[6-oxo-6-(undecyloxy)hexyl]amino]-octanoic acid, 1-octylnonyl ester (SM-102), and SM-102 N-oxide were purchased from Cayman Chemical Company, USA. Nexterion glass slides D uncoated (cleanroom cleaned) were obtained from Applied Microarrays, Inc., USA. Poly(dimethylsiloxane) monomer and curing agent were purchased from Dow Corning, USA. Polystyrene-*b*-poly(4-vinyl)pyridine ($PS_{48,400}$-*b*-$P4VP_{21,300}$, M_W/M_N = 1.09) was purchased from Polymer Source Inc., Canada. Aqueous solutions were prepared using deionized (DI) water (ρ ~ 18.2 MΩ cm) filtered by a Milli-Q water purification system (Millipore). Except where noted, all reagents and materials were used as received without further purification.

4.2 Fabrication of NEA devices

Two-electrode NEAs were fabricated using previously reported procedures (Fu et al., 2017; Ma et al., 2013). A 100 nm thick Au layer was sandwiched between 5 nm Ti layers on a cleanroom-clean glass slide using electron-beam evaporation (UNIVEX 450B, Oerlikon) to serve as the bottom electrode. Then, a 100 nm SiN_x layer was deposited by plasma-enhanced chemical vapor deposition (PECVD, Unaxis 790, Plasma-Therm). The Au top electrode was

deposited similarly, followed by deposition of 500 nm SiO_2 using PECVD. Nanosphere lithography (NSL) was utilized to define a dense nanopore array. Polystyrene beads (560 nm diam.) were mixed with ethanol in a 1:2 volumetric ratio and added dropwise to a water/air interface in a glass petri dish. Then, the beads were transferred to the substrate by emersing an O_2-plasma cleaned glass slide through the water/air interface, after which the mean particle size was reduced to 330 nm using isotropic O_2 plasma etching.

Subsequently, a 70 nm thick Cr layer was deposited as a hard photomask, and the beads were removed in acetone. The array was defined to a 100 μm x 100 μm square size using contact photolithography, and ring-disk nanopore electrodes were fabricated via sequential reactive-ion etching (RIE, Plasma-Therm 790) of SiO_2, Au, and SiN_x.

4.3 PS-b-P4VP membrane preparation and transfer

PS-*b*-P4VP membranes were prepared using either (1) direct spin-coating on planar Au electrodes, or (2) sacrificial membrane transfer for the preparation of BCP@NEA structures. For direct spin-coating, a 1,4-dioxane solution of 3 wt% PS_{48400}-*b*-PS_{21300} was spin-coated at 3000 rpm onto the substrate. To execute the sacrificial membrane transfer method, an aqueous solution of 5 wt% polyacrylic acid (PAA) was spin-coated at 4000 rpm onto an O_2 plasma-cleaned Si wafer. Then, a solution of 3 wt% PS_{48400}-*b*-PS_{21300} in 1,4-dioxane was spin-coated onto the PAA layer at 3000 rpm and dried under N_2. The layered substrate was immersed in pure ethanol for 15 s and dried under N_2. Afterward, the PAA layer was dissolved in a 1 mM phosphate buffer solution (pH = 7.4) until a free-standing BCP membrane emerged at the water-air interface. The membrane was then mechanically collected and placed onto an NEA device after emersion, and excess solution was removed with N_2, yielding hierarchically-organized BCP@NEA structures. BCP@NEA

devices were characterized after sputter coating the membrane with 1.5 nm Ir by focused ion-beam - scanning electron microscopy (FIB-SEM).

4.4 Electrografting of TBO on Au electrodes

Diazo-TBO compounds were synthesized by adding ice-cold $NaNO_2$ solution (1 mL, 40 mM) dropwise to an ice-cold solution of TBO (4 mL, 1.25 mM) in HCl (1 M) over the course of 5 min. The mixture was stirred for 30 min on ice and 100 µL of the crude reaction solution were afterwards placed in contact with the NEAs. The sensing electrode was poised at -0.6 V vs Ag/AgCl for 120 s to graft TBO onto the electrode, and unreacted crude reaction mixture was rinsed off using DI water. The resulting adsorbate coverage was characterized using IR spectroscopy and CV at varying scan rates.

4.5 Immobilization of ALDH

A 100 mM ethanolic solution of 3-mercaptopropionic acid (3-MPA) was incubated on a TBO-modified NEA device for 60 min and rinsed with ethanol and DI water. Subsequently, a solution containing 100 mM solution each of 1-ethyl-3-(3-dimethylaminopropyl)carbodiimide (EDC) and N-hydroxy succinimide (NHS) was placed on the device for 60 min. Afterward, a 0.3 mg/mL solution of yeast aldehyde dehydrogenase (>10 units/mg protein, EC number: 1.2.1.5, Sigma-Aldrich) in PBS (pH = 7.4) was drop-cast onto the device for an additional 60 min. The device was rinsed with PBS and a PS-*b*-P4VP membrane was placed onto the device using the previously described sacrificial membrane transfer to yield ALDH-functionalized BCP@NEA architectures.

4.6 Lipid nanoparticle synthesis and characterization

Lipids were dissolved in ethanol at a molar ratio of 50:10:38.5:1.5 (SM-102:1,2-DSPC:cholesterol:DMG-PEG(2000)) to a total lipid concentration of 10 mg/mL. The lipid solution was injected into 25 mM acetate buffer (pH = 5.3) at a 1:3 ratio under constant stirring at 300 rpm and the solution was continuously stirred for 30 min. Afterward, the resulting particles were left undisturbed for 60 min and the solution was dialyzed against PBS (pH = 7.4) using dialysis tubing (MWCO = 12.4 kDa) and stored at -20°C. Synthesized LNPs were characterized using dynamic light scattering (Nanotrac Wave II, Microtrac) utilizing a refractive index of 1.47 for the LNPs and 1.33 for the aqueous solution. The viscosity of the solution was set to 0.911 mPa s. The zeta potential was measured at an effective field strength of 8.7 kV/m.

4.7 Aldehyde detection on BCP@NEAs

Aldehydes were dissolved in PBS (pH = 7.4) containing 500 μM NAD^+ cofactor and placed on functionalized BCP@NEA sensors. For aldehydes exhibiting low solubility in aqueous media, 5% v/v acetonitrile was added as co-solvent. Mass transport into the pores was initiated by applying either a potential of -0.8 V vs Ag/AgCl or the extracted switching potential for non-aqueous solvent mixtures on the gating electrode for 30 s. Afterward, the solution was incubated for 5 min before conducting electrochemical measurements using the sensing electrode.

4.8 SM-102 N-oxide degradation and measurements

Commercially available ethanolic SM-102 N-oxide solutions (Cayman Chemical) were injected into 25 mM acetate buffer (pH = 5.3) at a 1:3 ratio and incubated at room temperature for 7 days. For electrochemical measurements, LNPs were spiked with incubated SM-102 N-oxide and NAD^+ in PBS (pH = 7.4), resulting in a final concentration of 500 μM NAD^+, and varying concentrations of N-oxide. For UV-vis measurements, PBS solutions containing degraded SM-

102 N-oxide, 500 μM NAD^+, and 0.3 mg/mL freely-diffusing ALDH were prepared and then adjusted to pH = 9.3 to allow for optimum enzyme conditions. The analyte solutions were placed in a 360 μL volume quartz cuvette, and the absorption at 340 nm was measured over time using an absorption spectrometer (Jasco V-670).

4.9 Electrochemical measurements

Electrochemical measurements were conducted on a multichannel CHI1030C electrochemical workstation (CH Instruments, USA). Ag/AgCl (1 M KCl) and a Pt wire were used as reference and counter electrodes, respectively, while the eight bottom electrodes of a single chip were simultaneously used as working electrodes. 100 μL volume analyte solutions were placed inside a PDMS reservoir, covering the BCP@NEAs. Cyclic voltammograms were collected using a scan rate of 100 mV/s unless otherwise noted. Amperometric measurements were conducted using the gating electrode and hydrophobic gating in BCP@NEA devices was enabled by poising the potential to -0.8 V vs Ag/AgCl for 30 s in aqueous solutions. In the presence of non-aqueous solvents, the switching potential was applied for 30 s. Square wave voltammograms were recorded using the bottom electrode as the working electrode with a pulse frequency of 50 Hz, a pulse amplitude of 100 mV, and a potential increment of 1 mV unless otherwise noticed. Peak currents in SWV were extracted after performing a constant background subtraction using the global minimum of the i-V response. For blank measurements, an empirical background correction was conducted by fitting three local points around the global minimum and the current between 0.3 V and 0.4 V to an exponential function, **Fig. S12**, to precisely determine the background current. Background subtractions were conducted using the *OriginPro Peak Analyzer* toolbox.

4.10 Determination of LODs

To determine the LOD, we utilized the linear increase in the calibration curves, as shown in **Fig. S13**, for the detection of benzaldehyde. Using the standard deviation of the blank and the slope of the initial linear increase at low concentrations, the LODs were calculated as LOD = $3.3\times\sigma_{blank}$/slope.

.

Acknowledgments

This work was supported by the NSF IUCRC Center for Bioanalytical Metrology through NSF grant IIP 1916601. The authors gratefully acknowledge Dr. Joseph Schariter (Moderna), Dr. Dipendra Gyawali (Moderna), and Dr. Christopher Welch (Indiana Consortium for Analytical Science) for their continuous support and advice throughout this project. We would also like to acknowledge the Notre Dame Nanofabrication Facility, the Notre Dame Integrated Imaging Facility, and the Notre Dame Materials Characterization Facility for their expert assistance in device fabrication and characterization.

Appendix A. Supplementary Data

Additional data supporting the text in the main article and experimental details, methods, and materials.

Keywords: Biosensors • Block copolymers • Electrochemistry • Lipid Nanoparticles • Nanopores

References

Arrigan, D.W.M., 2004. Nanoelectrodes, nanoelectrode arrays and their applications. Analyst 129 (12), 1157-1165.

Baden, L.R., El Sahly, H.M., Essink, B., Kotloff, K., Frey, S., Novak, R., Diemert, D., Spector, S.A., Rouphael, N., Creech, C.B., McGettigan, J., Khetan, S., Segall, N., Solis, J., Brosz, A., Fierro, C., Schwartz, H., Neuzil, K., Corey, L., Gilbert, P., Janes, H., Follmann, D., Marovich, M., Mascola, J., Polakowski, L., Ledgerwood, J., Graham, B.S., Bennett, H., Pajon, R., Knightly, C., Leav, B., Deng, W., Zhou, H., Han, S., Ivarsson, M., Miller, J., Zaks, T., 2020. Efficacy and Safety of the mRNA-1273 SARS-CoV-2 Vaccine. N. Engl. J. Med. 384 (5), 403-416.

Baek, S., Cutri, A.R., Han, D., Kwon, S.-R., Reitemeier, J., Sundaresan, V., Bohn, P.W., 2022. Multifunctional nanopore electrode array method for characterizing and manipulating single entities in attoliter-volume enclosures. J. Appl. Phys. 132 (17), 174501.

Bard, A.J., Faulkner, L.R., White, H.S., 2022. Electrochemical Methods: Fundamentals and Applications, 3rd ed. John Wiley & Sons.

Birdsall, R.E., Han, D., DeLaney, K., Kowalczyk, A., Cojocaru, R., Lauber, M., Huray, J.L., 2024. Monitoring stability indicating impurities and aldehyde content in lipid nanoparticle raw material and formulated drugs. J. Chromatogr. B 1234, 124005.

Chi, Y., Feng, Y., Wen, S., Lü, H., Yu, Z., Zhang, W., Sheng, G., Fu, J., 2007. Determination of carbonyl compounds in the atmosphere by DNPH derivatization and LC–ESI-MS/MS detection. Talanta 72 (2), 539-545.

Collins, G.C.S., George, W.O., 1971. Nuclear magnetic resonance spectra of glycolaldehyde. J. Chem. Soc. B (0), 1352-1355.

Cullis, P.R., Hope, M.J., 2017. Lipid Nanoparticle Systems for Enabling Gene Therapies. Mol. Ther. 25 (7), 1467-1475.

Douny, C., Bayram, P., Brose, F., Degand, G., Scippo, M.-L., 2016. Development of an LC-MS/MS analytical method for the simultaneous measurement of aldehydes from polyunsaturated fatty acids degradation in animal feed. Drug Test. Anal. 8 (5-6), 458-464.

Douny, C., Tihon, A., Bayonnet, P., Brose, F., Degand, G., Rozet, E., Milet, J., Ribonnet, L., Lambin, L., Larondelle, Y., Scippo, M.-L., 2015. Validation of the Analytical Procedure for the Determination of Malondialdehyde and Three Other Aldehydes in Vegetable Oil Using Liquid Chromatography Coupled to Tandem Mass Spectrometry (LC-MS/MS) and Application to Linseed Oil. Food Anal. Methods 8 (6), 1425-1435.

Estapé Senti, M., García del Valle, L., Schiffelers, R.M., 2024. mRNA delivery systems for cancer immunotherapy: Lipid nanoparticles and beyond. Adv. Drug Del. Rev. 206, 115190.

Eygeris, Y., Gupta, M., Kim, J., Sahay, G., 2022. Chemistry of Lipid Nanoparticles for RNA Delivery. Acc. Chem. Res. 55 (1), 2-12.

Fan, Y., Marioli, M., Zhang, K., 2021. Analytical characterization of liposomes and other lipid nanoparticles for drug delivery. J. Pharm. Biomed. Anal. 192, 113642.

Fu, K., Han, D., Ma, C., Bohn, P.W., 2017. Ion selective redox cycling in zero-dimensional nanopore electrode arrays at low ionic strength. Nanoscale 9 (16), 5164-5171.

Fu, K., Kwon, S.-R., Han, D., Bohn, P.W., 2020. Single entity electrochemistry in nanopore electrode arrays: ion transport meets electron transfer in confined geometries. Acc. Chem. Res. 53 (4), 719-728.

Gligor, D., Dilgin, Y., Popescu, I.C., Gorton, L., 2009. Poly-phenothiazine derivative-modified glassy carbon electrode for NADH electrocatalytic oxidation. Electrochim. Acta 54 (11), 3124-3128.

Guevara, M.L., Persano, F., Persano, S., 2020. Advances in Lipid Nanoparticles for mRNA-Based Cancer Immunotherapy. Front. Chem. 8.

Hald Albertsen, C., Kulkarni, J.A., Witzigmann, D., Lind, M., Petersson, K., Simonsen, J.B., 2022. The role of lipid components in lipid nanoparticles for vaccines and gene therapy. Adv. Drug Del. Rev. 188, 114416.

Hassett, K.J., Benenato, K.E., Jacquinet, E., Lee, A., Woods, A., Yuzhakov, O., Himansu, S., Deterling, J., Geilich, B.M., Ketova, T., Mihai, C., Lynn, A., McFadyen, I., Moore, M.J., Senn, J.J., Stanton, M.G., Almarsson, Ö., Ciaramella, G., Brito, L.A., 2019. Optimization of Lipid Nanoparticles for Intramuscular Administration of mRNA Vaccines. Mol. Ther. Nucleic Acids 15, 1-11.

Hou, X., Zaks, T., Langer, R., Dong, Y., 2021. Lipid nanoparticles for mRNA delivery. Nat. Rev. Mater. 6 (12), 1078-1094.

Houseley, J., Tollervey, D., 2009. The Many Pathways of RNA Degradation. Cell 136 (4), 763-776.

Jeschek, D., Lhota, G., Wallner, J., Vorauer-Uhl, K., 2016. A versatile, quantitative analytical method for pharmaceutical relevant lipids in drug delivery systems. J. Pharm. Biomed. Anal. 119, 37-44.

Kinsey, C., Lu, T., Deiss, A., Vuolo, K., Klein, L., Rustandi, R.R., Loughney, J.W., 2022. Determination of lipid content and stability in lipid nanoparticles using ultra high-performance liquid chromatography in combination with a Corona Charged Aerosol Detector. Electrophoresis 43 (9-10), 1091-1100.

Küchler, A., Yoshimoto, M., Luginbühl, S., Mavelli, F., Walde, P., 2016. Enzymatic reactions in confined environments. Nat. Nanotechnol. 11 (5), 409-420.

Liu, Z., Wang, W., Xie, R., Ju, X.-J., Chu, L.-Y., 2016. Stimuli-responsive smart gating membranes. Chem. Soc. Rev. 45 (3), 460-475.

Ma, C., Contento, N.M., Gibson, L.R., II, Bohn, P.W., 2013. Redox Cycling in Nanoscale-Recessed Ring-Disk Electrode Arrays for Enhanced Electrochemical Sensitivity. ACS Nano 7 (6), 5483-5490.

Melo Cardozo, I.M., Sousa, E.T., da Rocha, G.O., Pereira dos Anjos, J., de Andrade, J.B., 2020. Determination of free- and bound-carbonyl compounds in airborne particles by ultra-fast liquid chromatography coupled to mass spectrometry. Talanta 217, 121033.

Moiroux, J., Elving, P.J., 1980. Mechanistic aspects of the electrochemical oxidation of dihydronicotinamide adenine dinucleotide (NADH). J. Am. Chem. Soc. 102 (21), 6533-6538.

Musielak, E., Feliczak-Guzik, A., Nowak, I., 2022. Synthesis and Potential Applications of Lipid Nanoparticles in Medicine. Materials 15 (2), 682.

Ohtani, M., Kuwabata, S., Yoneyama, H., 1997. Electrochemical oxidation of reduced nicotinamide coenzymes at Au electrodes modified with phenothiazine derivative monolayers. J. Electroanal. Chem. 422 (1), 45-54.

Oude Blenke, E., Örnskov, E., Schöneich, C., Nilsson, G.A., Volkin, D.B., Mastrobattista, E., Almarsson, Ö., Crommelin, D.J.A., 2023. The Storage and In-Use Stability of mRNA Vaccines and Therapeutics: Not A Cold Case. J. Pharm. Sci. 112 (2), 386-403.

Packer, M., Gyawali, D., Yerabolu, R., Schariter, J., White, P., 2021. A novel mechanism for the loss of mRNA activity in lipid nanoparticle delivery systems. Nat. Commun. 12 (1), 6777.

Pardi, N., Tuyishime, S., Muramatsu, H., Kariko, K., Mui, B.L., Tam, Y.K., Madden, T.D., Hope, M.J., Weissman, D., 2015. Expression kinetics of nucleoside-modified mRNA delivered in lipid nanoparticles to mice by various routes. J. Control. Release 217, 345-351.

Pogocki, D., Schöneich, C., 2000. Chemical Stability of Nucleic Acid–Derived Drugs. J. Pharm. Sci. 89 (4), 443-456.

Polack, F.P., Thomas, S.J., Kitchin, N., Absalon, J., Gurtman, A., Lockhart, S., Perez, J.L., Pérez Marc, G., Moreira, E.D., Zerbini, C., Bailey, R., Swanson, K.A., Roychoudhury, S., Koury, K., Li, P., Kalina, W.V., Cooper, D., Frenck, R.W., Hammitt, L.L., Türeci, Ö., Nell, H., Schaefer, A., Ünal, S., Tresnan, D.B., Mather, S., Dormitzer, P.R., Şahin, U., Jansen, K.U., Gruber, W.C., 2020. Safety and Efficacy of the BNT162b2 mRNA Covid-19 Vaccine. N. Engl. J. Med. 383 (27), 2603-2615.

Powell, M.R., Cleary, L., Davenport, M., Shea, K.J., Siwy, Z.S., 2011. Electric-field-induced wetting and dewetting in single hydrophobic nanopores. Nat. Nanotechnol. 6 (12), 798-802.

Reichmuth, A.M., Oberli, M.A., Jaklenec, A., Langer, R., Blankschtein, D., 2016. mRNA vaccine delivery using lipid nanoparticles. Ther. Deliv. 7 (5), 319-334.

Reinhart, A.-G., Osterwald, A., Ringler, P., Leiser, Y., Lauer, M.E., Martin, R.E., Ullmer, C., Schumacher, F., Korn, C., Keller, M., 2023. Investigations into mRNA Lipid Nanoparticles Shelf-Life Stability under Nonfrozen Conditions. Mol. Pharm. 20 (12), 6492-6503.

Reitemeier, J., Baek, S., Bohn, P.W., 2023. Hydrophobic Gating and Spatial Confinement in Hierarchically Organized Block Copolymer-Nanopore Electrode Arrays for Electrochemical Biosensing of 4-Ethyl Phenol. ACS Appl. Mater. Interfaces 15 (33), 39707-39715.

Schoenmaker, L., Witzigmann, D., Kulkarni, J.A., Verbeke, R., Kersten, G., Jiskoot, W., Crommelin, D.J.A., 2021. mRNA-lipid nanoparticle COVID-19 vaccines: Structure and stability. Int. J. Pharm. 601, 120586.

Siriwardane, D.A., Wang, C., Jiang, W., Mudalige, T., 2020. Quantification of phospholipid degradation products in liposomal pharmaceutical formulations by ultra performance liquid chromatography-mass spectrometry (UPLC-MS). Int. J. Pharm. 578, 119077.

Smirnov, S.N., Vlassiouk, I.V., Lavrik, N.V., 2011. Voltage-Gated Hydrophobic Nanopores. ACS Nano 5 (9), 7453-7461.

U.S. Food & Drug Administration, 2018. Liposome Drug Products: Chemistry, Manufacturing, and Controls; Human Pharmacokinetics and Bioavailability; and Labeling Documentation. Available at: https://www.fda.gov/regulatory-information/search-fda-guidance-documents/liposome-drug-products-chemistry-manufacturing-and-controls-human-pharmacokinetics-and (Accessed 22 April 2024).

Vervoort, N., Daemen, D., Török, G., 2008. Performance evaluation of evaporative light scattering detection and charged aerosol detection in reversed phase liquid chromatography. J. Chromatogr. A 1189 (1), 92-100.

Wang, C., Sheng, Z.-H., Ouyang, J., Xu, J.-J., Chen, H.-Y., Xia, X.-H., 2012. Nanoconfinement Effects: Glucose Oxidase Reaction Kinetics in Nanofluidics. ChemPhysChem 13 (3), 762-768.

Wang, M.-F., Han, C.-L., Yin, S.-J., 2009. Substrate specificity of human and yeast aldehyde dehydrogenases. Chem.-Biol. Interact. 178 (1), 36-39.

Wang, S.-Y., Liu, H., Zhu, J.-H., Zhou, S.-S., Xu, J.-D., Zhou, J., Mao, Q., Kong, M., Li, S.-L., Zhu, H., 2022. 2,4-dinitrophenylhydrazine capturing combined with mass defect filtering strategy to identify aliphatic aldehydes in biological samples. J. Chromatogr. A 1679, 463405.

Yu, H., Qiu, X., Moreno, N., Ma, Z., Calo, V.M., Nunes, S.P., Peinemann, K.-V., 2015. Self-Assembled Asymmetric Block Copolymer Membranes: Bridging the Gap from Ultra- to Nanofiltration. Angew. Chem. Int. Ed. 54 (47), 13937-13941.

Zhong, Z., Ji, Q., Zhang, J.A., 2010. Analysis of cationic liposomes by reversed-phase HPLC with evaporative light-scattering detection. J. Pharm. Biomed. Anal. 51 (4), 947-951.

Table of contents graphic

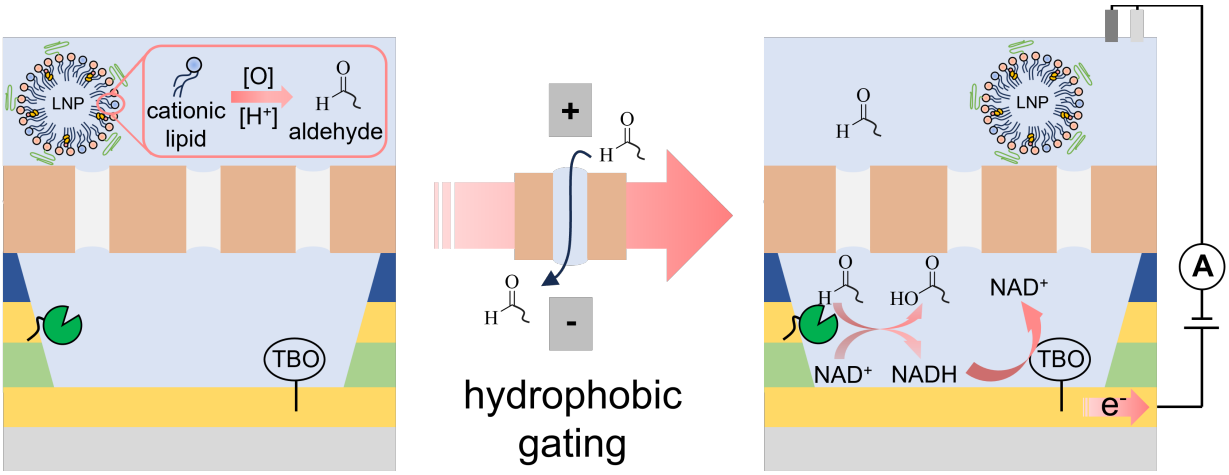

Supplementary data

Detection of aldehydes from degradation of lipid nanoparticle formulations using a hierarchically-organized nanopore electrochemical biosensor

Julius Reitemeier,[a] Jarek Metro,[a] and Paul W. Bohn[*a, b]

a Department of Chemistry and Biochemistry, University of Notre Dame, Notre Dame, Indiana 46556, United States

b Department of Chemical and Biomolecular Engineering, University of Notre Dame, Notre Dame, Indiana 46556, United States

[*]Author to whom correspondence should be addressed: *pbohn@nd.edu*

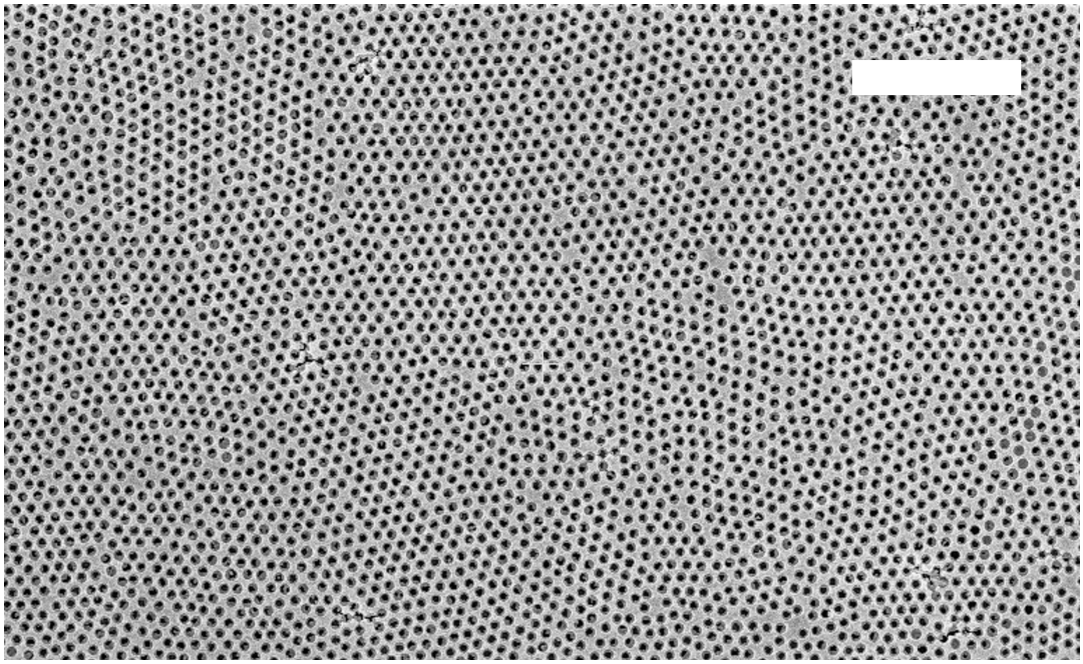

Fig. S1. Plan-view SEM image of an NEA prepared by nanosphere lithography and RIE showing the densely packed pore structure. Scale bar indicates 5 µm.

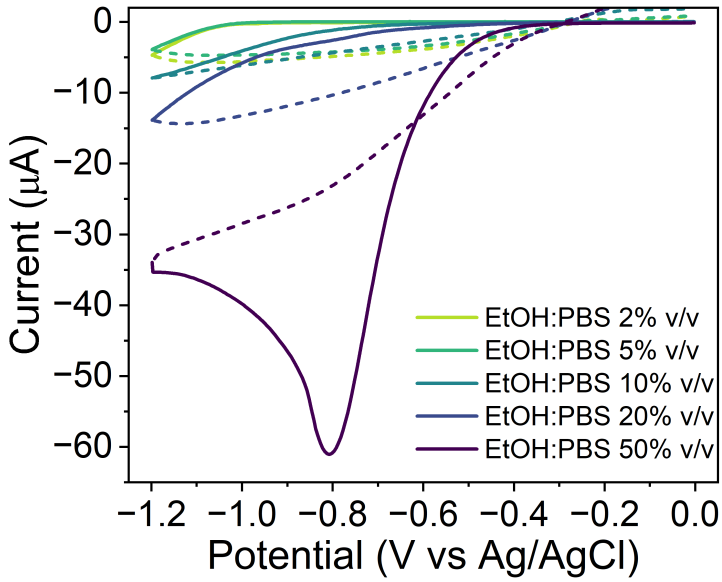

Fig. S2. CVs obtained in varying ethanol:PBS solvent compositions on a BCP-covered planar Au electrode. Analyte solution contained 5 mM $Fe(CN)_6^{3-/4-}$.

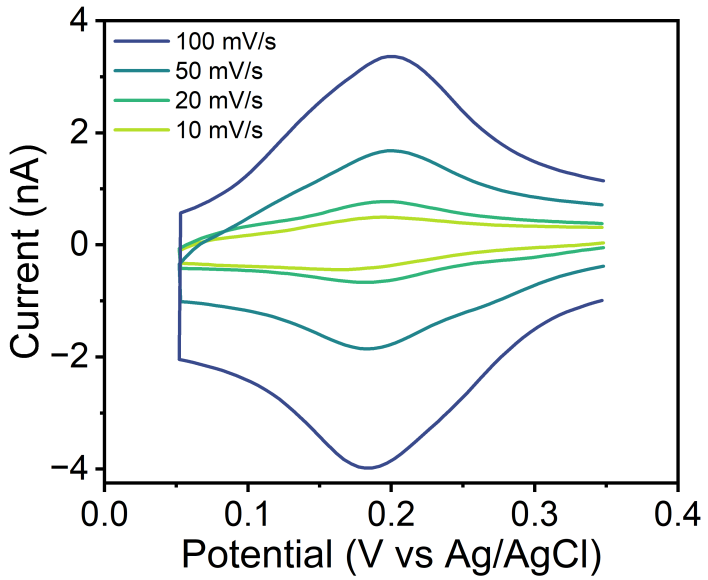

Fig. S3. CVs after hydrophobic gating on a BCP@NEA device in a 20% v/v ethanol:PBS mixture. The analyte solution contained 5 mM $Fe(CN)_6^{3-/4-}$.

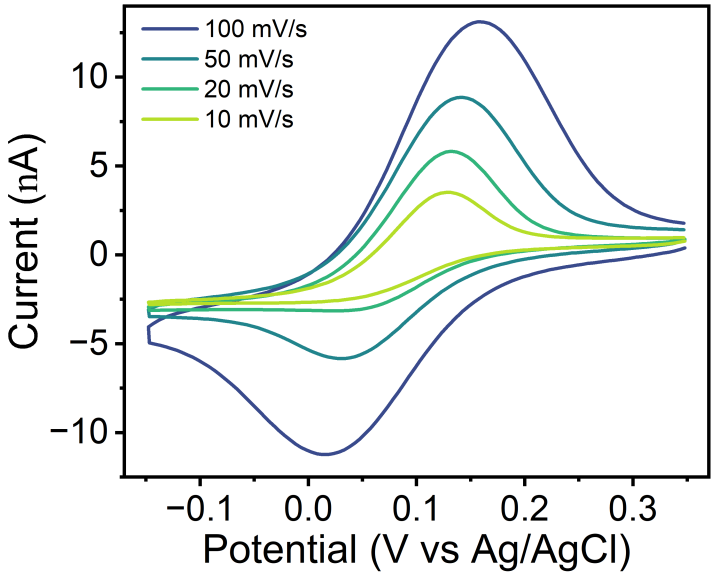

Fig. S4. CVs of 5 mM $Fe(CN)_6^{3-/4-}$ in 50% v/v acetonitrile:PBS obtained with varying scan rates after hydrophobic gating. The CVs show clear deviation from thin-layer cell behavior.

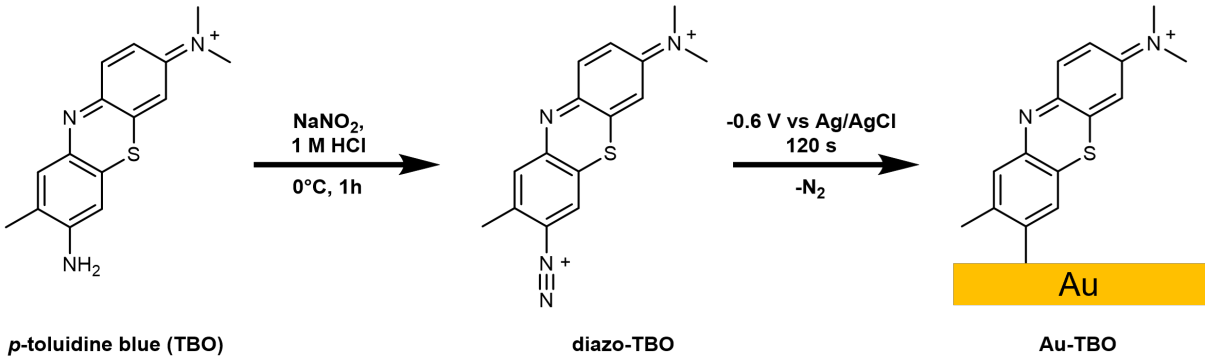

Fig. S5. Reaction scheme for electrografting of the diazo-TBO compound onto a Au electrode by applying a reducing potential for 120 s after immersion in the crude reaction mixture.

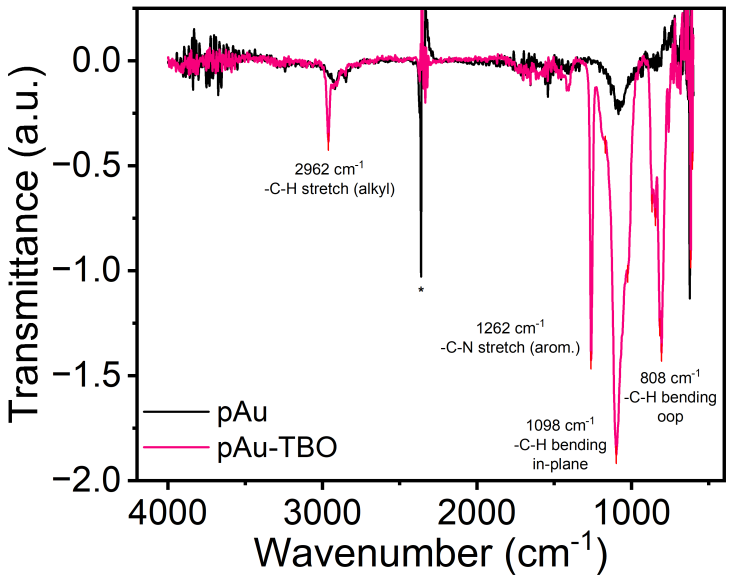

Fig. S6. Background corrected IR transmittance spectrum before and after electrografting of the redox mediator TBO on a planar Au electrode. The vibrational peaks between 1500 – 600 cm^{-1} show the C-N and C-C vibrations of the heteroaromatic compound. * Denotes artifact from ambient CO_2 correction.

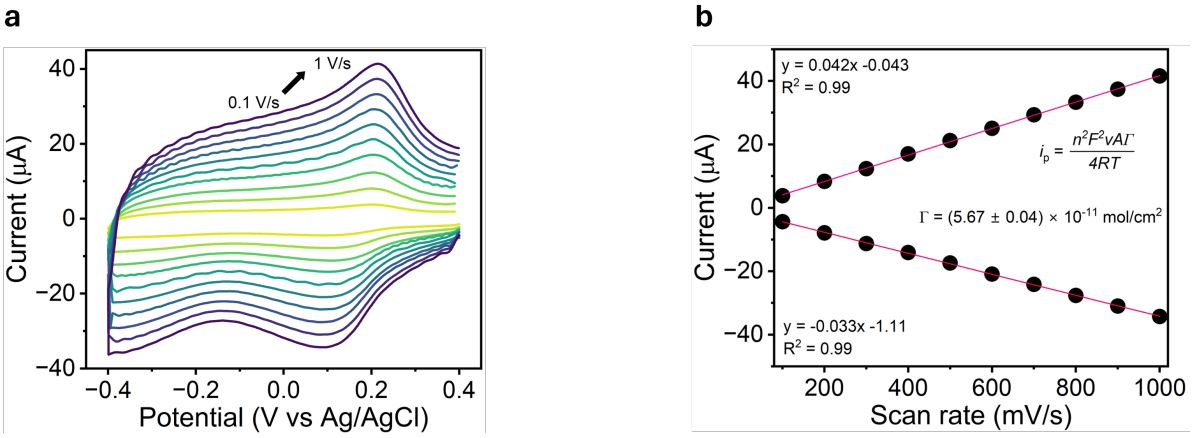

Fig. S7. Characterization of TBO coverage after electrografting on a planar Au electrode. **a** CVs at increasing scan rates from 0.1 - 1.0 V s^{-1}. **b** Peak currents on anodic (top) and cathodic (bottom) scans. CVs were obtained in PBS (pH =7.4) on an electrode area of A = 0.196 cm^2.

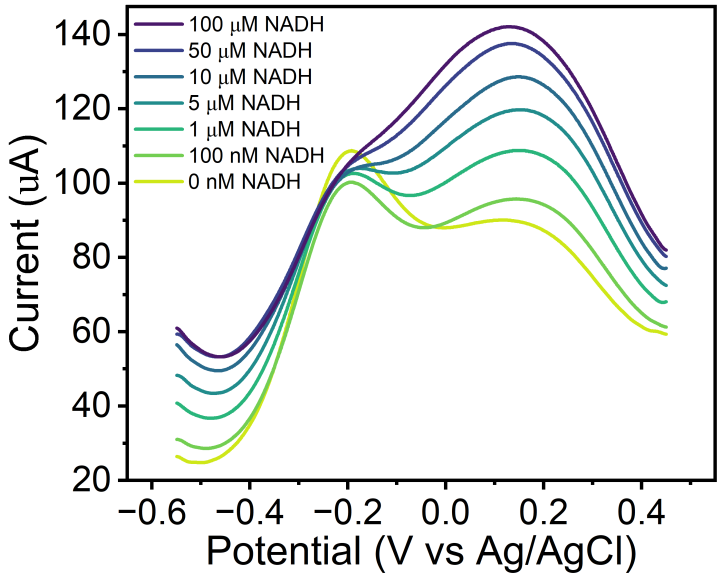

Fig. S8. SWVs (50 Hz, 100 mV) of NADH at varying concentrations in PBS. The SWV data indicate effective mediation of NADH oxidation by TBO-modified Au.

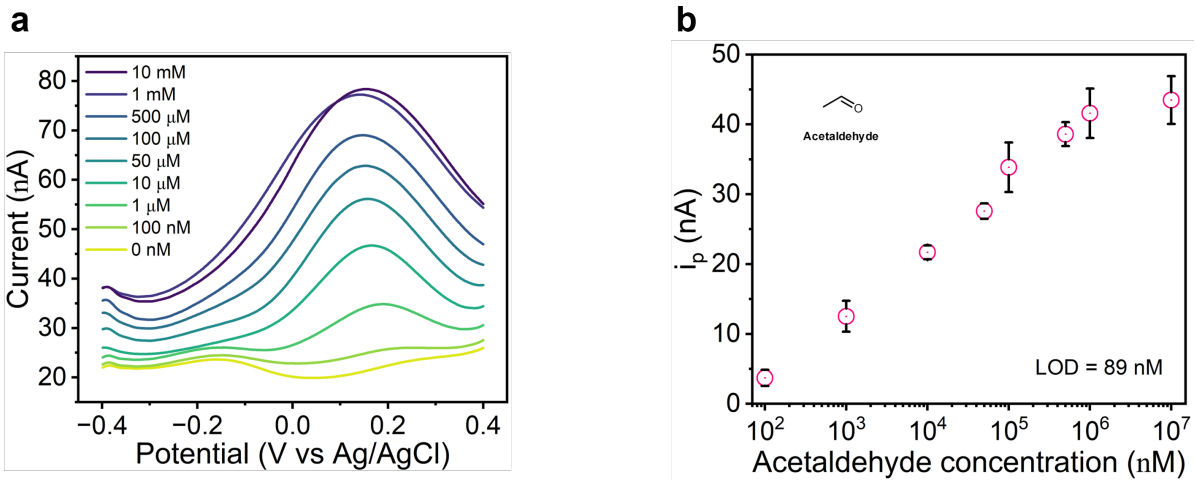

Fig. S9. Detection of acetaldehyde on BCP@NEA sensors. **a** SWVs of varying concentrations of acetaldehyde in the presence of 500 µM NAD^+ in PBS (pH = 7.4). **b** The corresponding working curve obtained from the SWV measurements. Error bars indicate the standard deviation across n = 3 replicates.

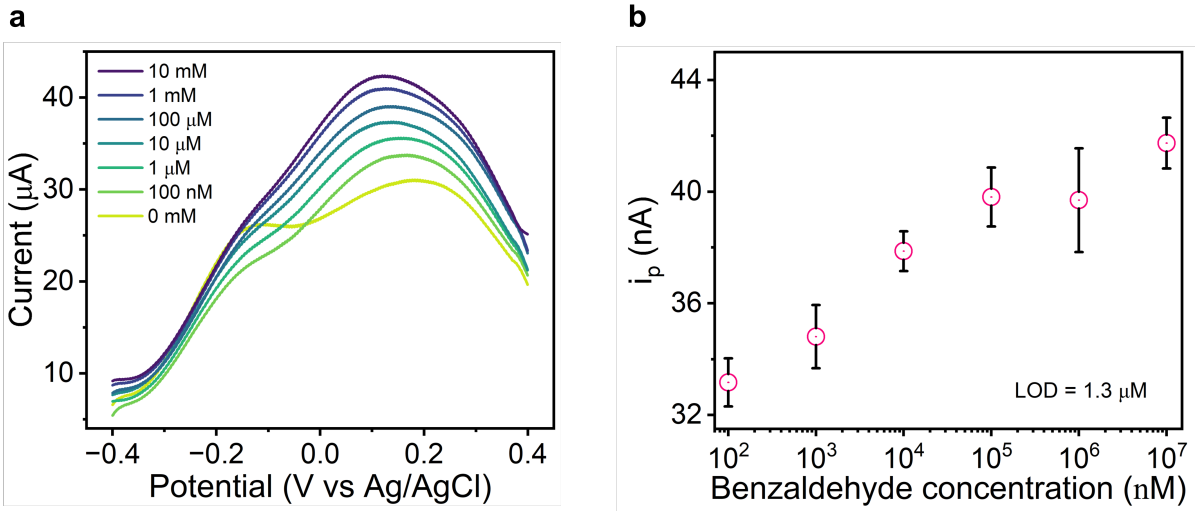

Fig. S10. Detection of acetaldehyde in open NEAs without the application of a BCP membrane. **a** SWVs of varying concentrations of acetaldehyde in the presence of 500 µM NAD^+ in PBS (pH = 7.4). **b** The corresponding working curve obtained from the SWV measurements. Error bars indicate the standard deviation across n = 3 replicates.

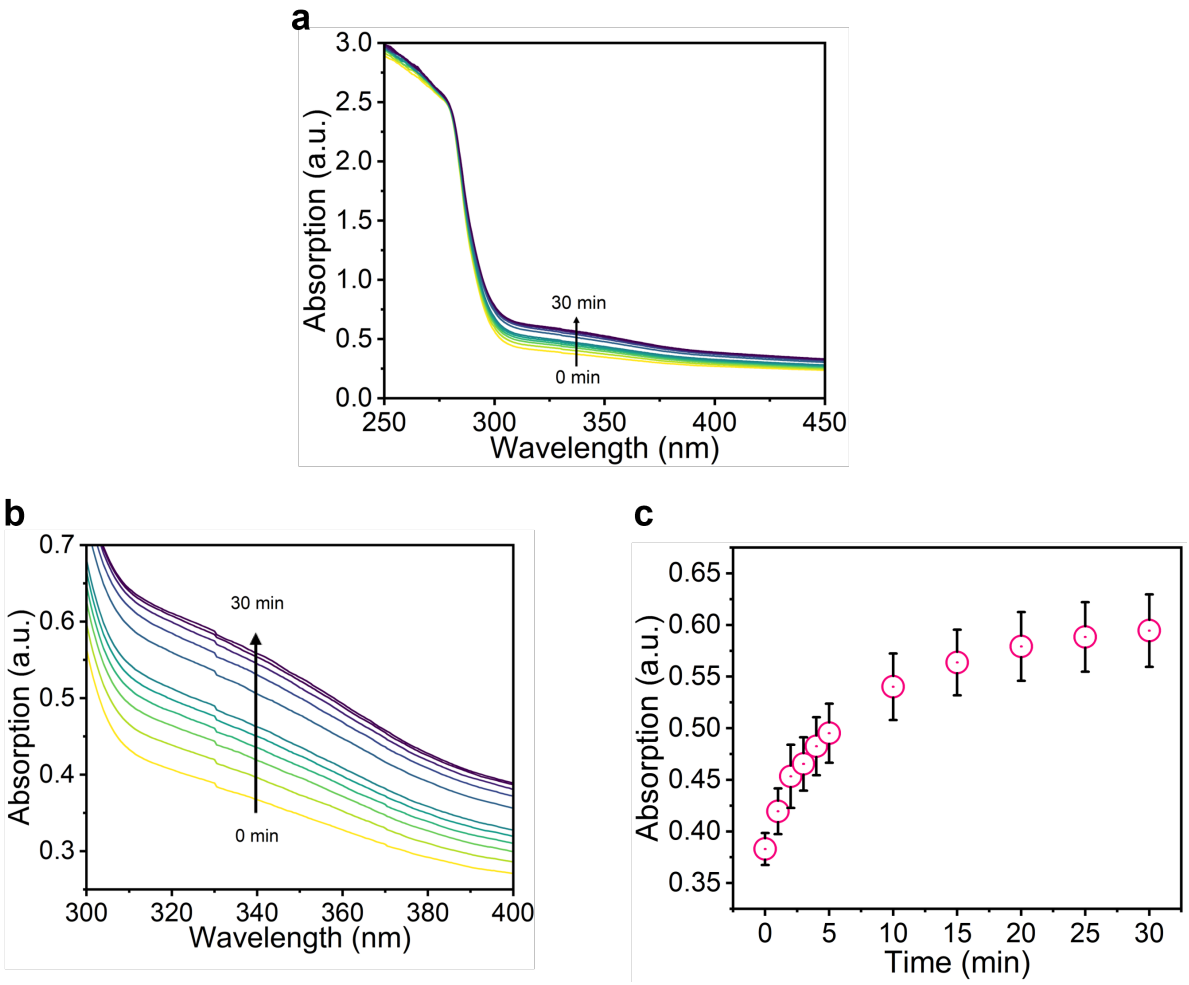

Fig. S11. UV-vis analysis of 1 mM degraded SM-102 N-oxide. **a** UV-vis spectra obtained over the course of 30 min. The analyte solution contained 0.3 mg/mL ALDH and 500 µM NAD^+ in basic PBS (pH = 9.3). **b** Magnified UV-vis spectra from **a** showing development of the NADH absorption band at 340 nm. **c** Progression curve obtained from the change in absorption at 340 nm over the course of 30 min. Error bars represent the standard deviation across n = 3 replicates.

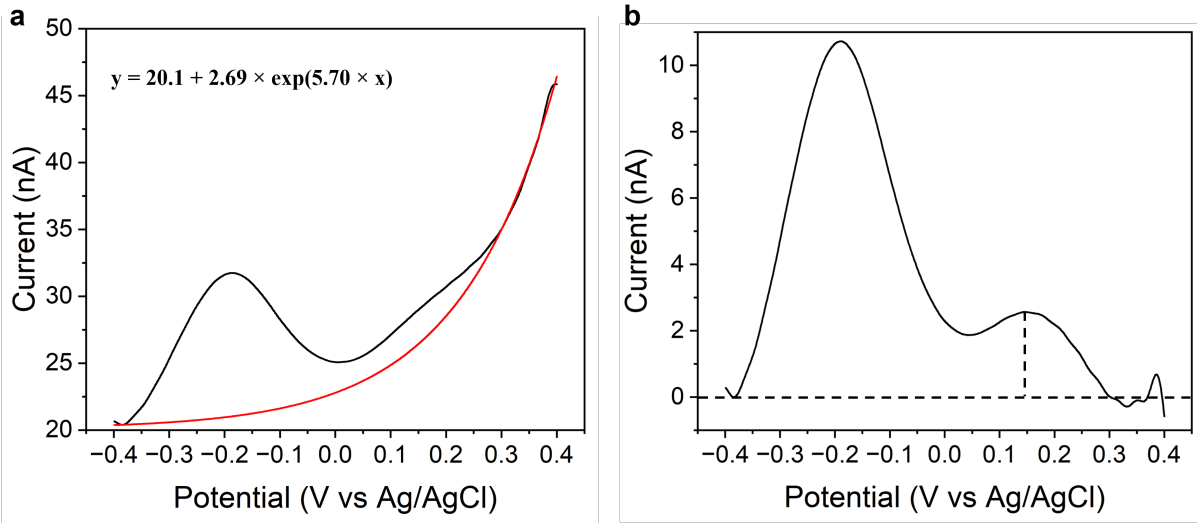

Fig. S12. Empirical background correction for SWV current response in the absence of aldehydes. **a** Exponential background fit using three local points around the global minimum and the current between 0.3 V and 0.4 V. **b** Background subtracted data and indicated peak current extraction.

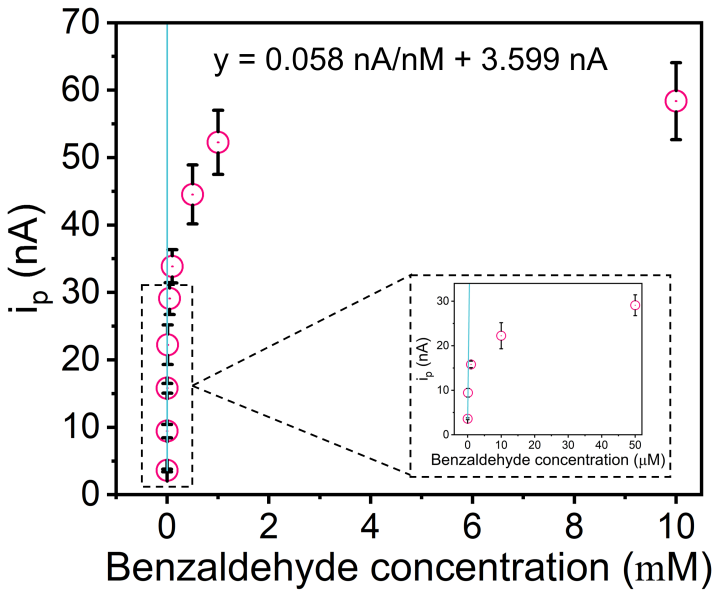

Fig. S13. Linear calibration curve of benzaldehyde using a BCP@NEA sensor. The LOD was determined using the slope of the initial linear increase in current at low concentrations and the standard deviation of the blank.